UV Photodissociation Dynamics of CD 3 SOCD 3 : Photofragment Translational and Internal Energy Distribution †

5 AUTHORS, INCLUDING:

Gustavo A Pino
Universidad Nacional de Córdoba and CONIC…
35 PUBLICATIONS   **327** CITATIONS

SEE PROFILE

Isayana Torres
Universidad Nacional de Ingeniería (Nicaragua)
40 PUBLICATIONS   **1,511** CITATIONS

SEE PROFILE

UV Photodissociation Dynamics of CD₃SOCD₃: Photofragment Translational and Internal Energy Distribution[†]

G. A. Pino, I. Torres, G. A. Amaral, F. J. Aoiz, and L. Bañares*

Departamento de Química Física I. Facultad de Química. Universidad Complutense, Madrid 28040, Spain

Received: February 17, 2004; In Final Form: March 23, 2004

The photodissociation of CD₃SOCD₃ (DMSO-d_6) has been studied at four different wavelengths in the UV region (204−227 nm) using resonance enhanced multiphoton ionization (REMPI) and time-of-flight mass spectrometry (TOFMS) to measure TOF profiles and rotational and vibrational REMPI spectra of the CD₃ photoproduct. Three dissociation channels producing CD₃ fragments have been identified. The major primary channel proceeds via internal conversion to the ground state followed by unimolecular decomposition, and it is characterized by an isotropic statistical translational energy distribution. Internally hot CD₃SO(X̃) fragments subsequently decompose over an exit barrier (45 ± 2 kJ mol⁻¹) to produce CD₃ and SO. Another primary channel results from a fast dissociation (direct dissociation or predissociation) that yields anisotropic CD₃ and presumably electronically excited CD₃SO(Ã) fragments with $\beta = 0.30 \pm 0.05$. In this last case, the fraction of available energy channeled into translation ($\langle f_t \rangle \approx 0.62$) is consistent with a soft impulsive model. The measured rotational spectra confirm the results obtained from the TOF profiles simulations.
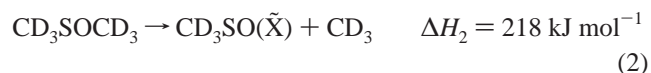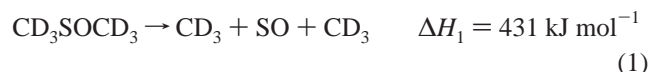
I. Introduction

Photodissociation of polyatomic molecules generally involves more than one product channel resulting from the multidimensional nature of the excited potential energy surfaces involved and from the efficient energy redistribution between the internal degrees of freedom of the parent molecule. In this sense, there has been recent interest in the mechanism of three-body fragmentation, particularly when the dissociation involves the breaking of two identical chemical bonds. When a molecule with two equivalent bonds is electronically excited with sufficient energy to break both bonds, how the rupture of the two bonds is temporally coupled becomes a salient question. If the departure of the two fragments takes place simultaneously, the mechanism is concerted, but if the cleavage of the bonds occurs in two sequential steps, with the lifetime of the intermediate exceeding its rotational period, the mechanism is stepwise.[1] The question of concerted versus stepwise dissociation still remains without answer for most of the systems, but recently this point has been addressed for acetone by North et al.[2] However, with the advent of time-resolved experiments with femtosecond time resolution, cases have been found where the above criterion based on the rotational period of the intermediate seems not to be valid, the comparison of the intermediate lifetime to the vibrational period along the reaction coordinate being the adequate definition for concertedness.[3]

Dimethyl sulfoxide (DMSO) is the sulfur analogue of acetone. Because DMSO is the simplest alkyl sulfoxide, its photochemistry represents a model system for the understanding of sulfoxide photochemistry and a good candidate to discriminate between the two dissociation mechanisms mentioned above. Understanding the photodissociation dynamics of this molecule is important not only because it presents very interesting photochemical properties but also because DMSO plays an important role in the atmospheric sulfur cycle as a possible intermediate in the oxidation of alkyl sulfides to sulfur dioxide.[4]

The energy of one photon in the UV region is high enough to break both C−S bonds in the DMSO-d_6 molecule. (By DMSO-d_6 we denote the fully deuterated species CD₃SOCD₃; that is the molecule studied in the present work. DMSO-h_6 corresponds to the undeuterated species.) Thus the two-methyl formation can proceed either via a concerted or stepwise dissociation mechanism:[5]

$$CD_3SOCD_3 \rightarrow CD_3 + SO + CD_3 \qquad \Delta H_1 = 431 \text{ kJ mol}^{-1} \tag{1}$$

$$CD_3SOCD_3 \rightarrow CD_3SO(\tilde{X}) + CD_3 \qquad \Delta H_2 = 218 \text{ kJ mol}^{-1} \tag{2}$$

$$CD_3SO(\tilde{X}) \rightarrow CD_3 + SO \qquad \Delta H_3 = 213 \text{ kJ mol}^{-1} \tag{3}$$

The DMSO-h_6 absorption spectrum in the UV region was first obtained by Gollnick and Stracke.[6] Three electronic transitions were identified: a band peaking at around 188 nm assigned to a localized $\pi^* \leftarrow \pi$ transition in the SO group, an absorption centered at 205 nm to a $\sigma^* \leftarrow n$ or $d \leftarrow n$ transition, and finally, a small band at about 220 nm assigned to a $\pi^* \leftarrow n$ transition. Figure 1 shows the absorption spectrum of DMSO-d_6 in the gas-phase deconvoluted in the three electronic transitions mentioned above, as well as the photodissociation wavelengths studied in the present work.

Four of the previous studies on DMSO photodissociation were carried out on the first absorption band at 193 nm.[7−10] In the first work performed at this wavelength, Chen et al.[7] used resonance enhanced multiphoton ionization (REMPI) to determine the internal energy of the CH₃ fragment and laser induced fluorescence (LIF) to obtain the SO quantum yield ($\Phi_{SO} = 1.02$) and its rovibrational energy distribution. Based mainly on the SO quantum yield measurement and its inverted vibrational
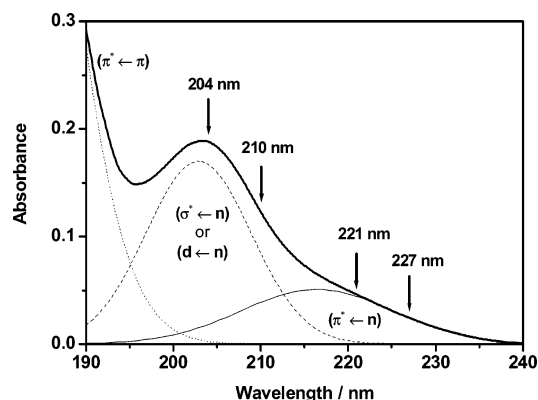
Figure 1. Gas-phase DMSO-d_6 absorption spectrum (bold solid line) deconvoluted in three electronic transitions: (solid line) not allowed $\pi^* \leftarrow n$ transition; (dashed line) either $\sigma^* \leftarrow n$ or $d \leftarrow n$ allowed transition; (dotted line) $\pi^* \leftarrow \pi$ allowed transition (see text for details). Arrows in the figure indicate the photolysis wavelengths studied in this work.

population, these authors suggested a concerted mechanism for the double S−C rupture.

Later, Zhao et al.[8] also studied DMSO dissociation at 193 nm by means of photofragment translational spectroscopy (PTS). In addition to CH_3 and SO, CH_3SO was also observed as a stable primary product, indicating that reaction 2 is an important channel. The quantum yield of CH_3 was determined to be $\Phi_{CH_3} = 1.53$. These results together with the analysis of the time-of-flight (TOF) data led the authors to conclude that SO is formed via a stepwise mechanism.

Subsequently, PTS experiments by Blank et al.[9] on DMSO-h_6 and DMSO-d_6 photodissociation at 193 nm led to the same conclusions but, in addition, these authors found evidence for the opening of a third channel producing $CD_3(CH_3)$. The two possible initial S−C bond cleavage pathways were reaction 2 and

$$CD_3SOCD_3 \rightarrow CD_3SO(\tilde{A}) + CD_3 \qquad (4)$$
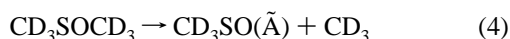
The major channel (2) was believed to proceed from the electronic ground state of DMSO after internal conversion (IC) from the electronically excited state, whereas the minor channel (4) was thought to proceed from an excited state, resulting in the formation of electronically excited $CD_3SO(\tilde{A})$. The authors expected this channel to be rapid (prompt or fast electronic predissociation); however, the experimental technique was not sensitive enough to detect any type of anisotropy in the signal. According to these authors, the electronically excited $CD_3SO(\tilde{A})$ fragment did not further dissociate, but $\Phi_{CD_3(CH_3)}$ was found to be larger than 1 (1.4 and 1.53 for CD_3 and CH_3, respectively), as a consequence of the subsequent decomposition of the CD_3-$SO(\tilde{X})/CH_3SO(\tilde{X})$ fragment (reaction 3) arising from the ground-state dissociation of the parent molecule (reaction 2).

Rudolph et al.[10] used infrared diode laser absorption spectroscopy to detect the CD_3 photoproducts formed in the 193 and 222 nm photodissociation of DMSO-d_6. Φ_{CD_3} was determined to be 1.4 at 193 nm and 1.2 at 222 nm, indicating partial secondary decomposition of the CD_3SO product. No direct evidence of reaction 4 was found either at 193 nm or at 222 nm. Nevertheless, in both cases the results were in good agreement with a stepwise mechanism.

More recently, Thorson et al.[11] performed photodissociation studies at 210 and 222 nm, using VUV light coupled to TOF spectrometry for photofragments detection and analysis. These authors also determined the SO internal energy by means of

LIF spectroscopy. The Φ_{CH_3} measured at 222 nm was 1.1 ± 0.1, in good agreement with the value reported by Rudolph et al.,[10] whereas Φ_{CH_3} was 1.3 ± 0.1 at 210 nm.

In a previous study in our laboratory, the photodissociation of DMSO-d_6 at 210 nm was studied using the REMPI-TOF technique to determine the translational energy of the CD_3 fragments.[12] From these experiments, clear evidence for an anisotropic CD_3 channel was obtained. CD_3 product TOF profile analysis indicated that the anisotropic signal arose from reaction 4, in agreement with Blank et al.[9]

In the present work, the results obtained at four different photolysis wavelengths, 204, 210, 221, and 227 nm, are presented. The REMPI-TOFMS technique has been used to determine the internal and translational energy of the CD_3 fragment at each wavelength. The anisotropy parameter and the Φ_{CD3} have been measured and a general mechanism for the photodissociation of DMSO-d_6 has been proposed.

II. Experimental Section

The experimental system has been described in detail elsewhere.[13] Briefly, it consists of a supersonic jet chamber (10^{-6} Torr, under operational conditions) where a jet is entrained perpendicular to the laser beams as well as the TOF direction toward a microchannel plate (MCP) detector. Two, linearly polarized, counterpropagating laser beams (photodissociation or pump beam and probe or REMPI beam) intersect with the pulsed jet at the ionization point. Ions are extracted from the interaction region using continuous voltages applied to a series of stainless steel plates that are arranged in a Wiley−McLaren type setup under space focusing conditions.[14]

The supersonic jet beam is produced by the co-expansion of DMSO-d_6 (Aldrich, 99.0%, room temperature) and He through a pulsed valve (General Valve, No. 9) 0.5 mm diameter nozzle, into the chamber. The stagnation pressure was about 200 Torr. The jet is intercepted first by the pump beam, and 18−90 ns later it is then intercepted by the probe beam which ionizes the CD_3 fragments via 2+1 REMPI on the $4p_z$ or $3p_z$ ($^2A_2'' \leftarrow \tilde{X}^2A_2''$) transitions. The photolysis laser is fired at an optimal time ($\sim 200 \ \mu s$) after the pulsed valve, interacting with the early edge of the jet such that cluster formation is minimized. The photolysis laser is the frequency-mixed output of a 532 nm Nd: YAG (Quanta Ray Pro 230) laser-pumped dye laser (Continuum ND 60) operating at 612−681 nm. The probe laser is the frequency-doubled tunable output of a 532 nm Nd:YAG (Continuum NY 81) laser-pumped dye laser (Continuum ND 60) operating around 573.3 or 667.8 nm depending on the CD_3 REMPI transition analyzed. The pump laser polarization plane can be rotated by inserting a double Fresnel rhomb in the beam path before entering the jet chamber. Typically, the photodissociation laser was used at energies lower than 10 μJ/pulse focused to a spot of ≈ 0.2 mm diameter, whereas the probe laser was used at energies of 300−600 μJ/pulse focused to a spot of ≈ 0.3 mm diameter. Both lasers and the pulsed valve were operated at a frequency of 10 Hz.

III. Results and Analysis

A. Energetics and Observed Fragments. At the photolysis wavelengths used in this work, the photon energy is high enough to open several fragmentation channels. Figure 2 shows the energy diagram containing the two reactive channels under discussion in the present study. However, as shown in Figure 3, other different channels are open and many ion fragments are present in the mass spectrum when the pump and probe lasers overlap in time.
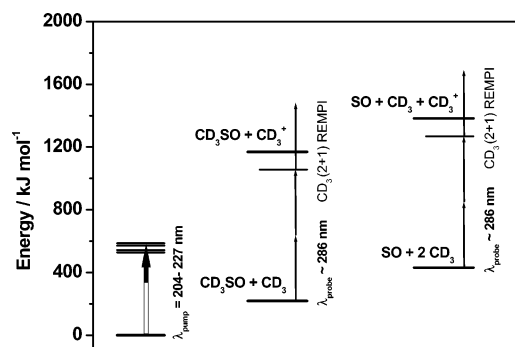
8050 *J. Phys. Chem. A, Vol. 108, No. 39, 2004*

Pino et al.

Figure 2. Energy level diagram of the two dissociation channels studied in this work producing CD_3 fragments. The detection REMPI scheme of the CD_3 photofragment for the $4p_z\ ^2A_2'' \leftarrow \tilde{X}^2A_2''$ transition is also displayed.
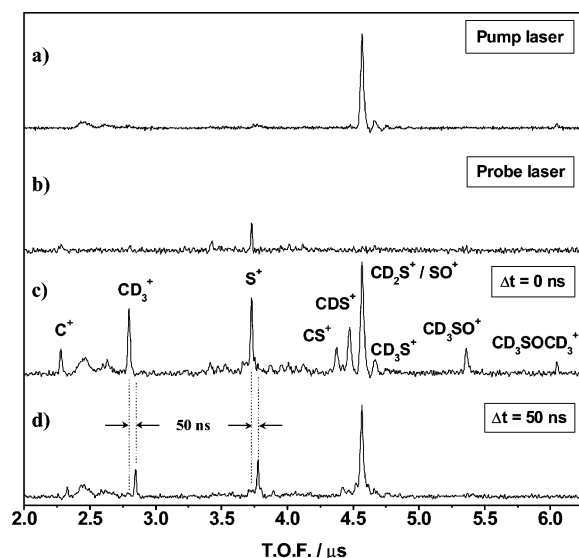

Figure 3. (a) Mass spectrum after ionization with pump laser at 221 nm. (b) Mass spectrum after ionization with probe laser tuned at the R(5) rotational line of the CD_3 photofragment. (c) Pump−probe mass spectrum at zero time delay. (d) Pump−probe mass spectrum at 50 ns time delay between pump and probe lasers. In all cases the pump laser energy was 20 μJ/pulse and the probe laser energy 500 μJ/pulse.

Figure 3a shows the mass spectrum obtained with the pump laser tuned at 221 nm (energy below 20 μJ/pulse) and the probe laser off. The spectrum is dominated by the peak corresponding to SO^+/CD_2S^+ and the parent ion $(CD_3)_2SO^+$ is barely observed. With only the probe laser fired (energy below 500 μJ/pulse), S^+ is the only fragment ion observed in the spectrum, as shown in Figure 3b. In this case the probe laser was tuned to the R(5) rotational line of the $CD_3\ 0_0^0\ 4p_z\ (^2A_2'' \leftarrow \tilde{X}\ ^2A_2'')$ transition. Figure 3c shows the pump−probe mass spectrum, under the same conditions mentioned above, at zero time delay, $\Delta t = 0$, between the pump and probe lasers. Additional fragment ions corresponding to C^+, CD_3^+, CS^+, CDS^+ and CD_3SO^+ are detected, and the intensity of the S^+, $(CD_3)_2SO^+$ and SO^+/CD_2S^+ signals increases with respect to that shown in Figure 3a,b. When Δt increases to 50 ns (Figure 3d), this pump−probe effect disappears for all masses except that of CD_3^+, whose intensity decreases. This behavior was also observed in our previous study at 210 nm.[12] When both lasers overlap in time, there is a pump−probe multiphoton absorption process giving rise to all fragment ions mentioned above, which, in turn, strongly decreases when Δt increases over 15 ns. CD_3^+ is the only pump−probe signal that does not disappear as Δt increases. This fact, together with the observed linear dependence of the

CD_3^+ signal with the pump laser energy, measured at $\Delta t = 18$ ns, indicates that only neutral CD_3 fragments are formed by the photolysis laser, which are later ionized solely by the probe laser under the present experimental conditions. This effect was observed at the four photolysis wavelengths used in the present work. It must be pointed out that CD_3^+ is the only resonant peak within the probe laser wavelength range (285.5−287 nm).

A time delay of 18 ns was used in all the experiments to avoid multiphoton processes that could mask the neutral CD_3 fragments arising from reactions 1−4. At the same time, this relatively short Δt guarantees that even the fastest CD_3 neutral fragments do not escape from the ionization region before the probe laser arrives.[12] Moreover, the CD_3^+ signal dependence at $\Delta t > 18$ ns is linear only for laser energies below 20 μJ/ pulse; for that reason the pump laser energy was always kept ≤ 10 μJ/pulse.

B. CD₃ Fragment TOF Profiles: Translational Energy and Anisotropy. TOF profiles were recorded at the four photolysis wavelengths of this study with the probe laser tuned to the Q branch of the $CD_3\ 0_0^0\ 4p_z$ transition, where the signal intensity is enhanced by a factor of 30−40 with respect to the nonresonant multiphoton fragments, and for parallel and perpendicular polarization of the photolysis laser with respect to the TOF axis.

The widths of the features in the TOF mass spectrum reveal the recoil energy of the detected fragments. A fairly low extraction field (between 50 and 60 V/cm) was used to optimize the energy resolution without losing more than 1.5% of the ions in their trajectory to the detector as predicted by ion trajectory simulations using the SIMION 6.0[15] program. Special care was taken in the measurements to ensure that the difference in the area of the integrated TOF profiles at each photolysis laser polarization was not larger than 1.5%, to achieve identical or similar detection sensitivities, thus avoiding any further normalization.

The raw TOF profiles were slightly asymmetric about the center, t_0. A symmetrization procedure was applied by averaging the left and right parts of each profile with respect to t_0 to obtain symmetric TOF profiles. Figures 4 and 5 show the experimental symmetrized TOF profiles measured at mass 18 using parallel and perpendicular polarized photolysis light with respect to the detection axis at the four photolysis wavelengths studied. The TOF profiles for parallel and perpendicular polarization differ at the extremes of the profile, suggesting an anisotropic behavior for those CD_3 fragments arriving at small $(t - t_0 < 0)$ and large $(t - t_0 > 0)$ times. These ions correspond to CD_3 fragments with a maximum Z-axis velocity component $|v_Z|$ (initially flying directly toward or opposite to the detector on the Z-axis). It must be noted that the same anisotropic behavior was observed at *both* ends of the raw (asymmetric) TOF profiles, because the symmetrization procedure does not introduce any systematic error, as will be explained below. No effects on the TOF profiles were observed when the polarization of the probe laser was varied.

In the present experiments an actual anisotropy parameter β cannot be determined for the whole range of speeds because the anisotropy is determined as a function of v_Z instead of v. However, we can define an "anisotropy function", $\tilde{\beta}(t-t_0)$, as

$$\tilde{\beta}(t-t_0) = \frac{2[I_\parallel(t-t_0) - I_\perp(t-t_0)]}{[I_\parallel(t-t_0) + 2I_\perp(t-t_0)]} \quad (5)$$

where $I_\parallel(t-t_0)$ and $I_\perp(t-t_0)$ refer to the signal intensity as a function of time-of-flight when the pump laser is polarized
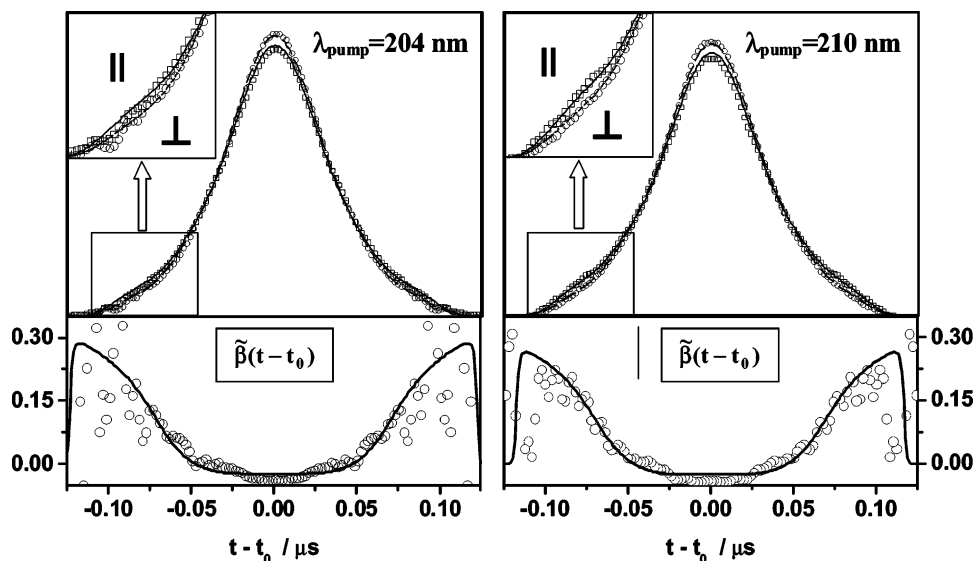
Figure 4. (Top panels) experimental (symbols) and simulated (lines) TOF profiles of the Q 0_0^0 line of the CD$_3$ $4p_z$ $^2A_2''$ ← $\tilde{X}^2A_2''$ transition after photodissociation of DMSO-d_6 at 204 nm (left) and 210 nm (right), using perpendicular (circles and dashed line) or parallel (square and solid line) polarized photolysis light. The small square on the top left part of the figures zooms in the signal portion corresponding to fast ions directed initially to the detector. (Bottom panels) velocity dependent "anisotropy function" calculated with eq 5 using the experimental (circles) and simulated (solid line) TOF profiles.
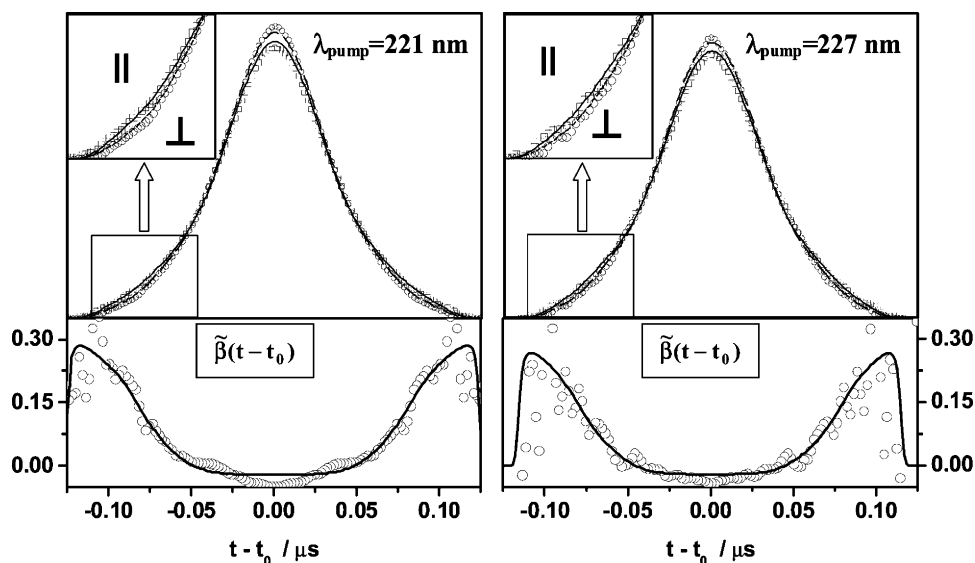

Figure 5. Same as Figure 4, but at 221 nm (left) and 227 nm (right).

parallel and perpendicular to the Z-axis, respectively. The physical meaning of $\tilde{\beta}(t-t_0)$ is that of the average β over all speeds, v, with a given v_Z projection. Therefore, only for those fragments arriving at the largest $|t - t_0|$, where $v_Z \approx v$, are the values of $\tilde{\beta}(t-t_0)$ a good approximation to the actual values of the anisotropy parameter β. Then, a negative value of $\tilde{\beta}(t-t_0)$ around $|t - t_0| \approx 0$ does not necessarily imply a negative value of the β parameter.

The lower panels in Figures 4 and 5 show the $\tilde{\beta}(t-t_0)$ function obtained at each photolysis wavelength. The fact that the maximum value of $\tilde{\beta}(t-t_0)$ when $v_Z \approx v$ is positive indicates that some of the CD$_3$ fragments are generated anisotropically by a fast dissociation process corresponding to a parallel transition.

For a single speed distribution of the neutral fragments in the center-of-mass (CM) frame, $g(v)$, and in the absence of angular momentum alignment of the fragments, the projected velocity distribution on the detector axis observed experimen-

tally, $f(v_Z,\theta)$, is given by

$$f(v_Z,\theta) = \int_{|v_Z|}^{v_{max}} \frac{g(v)}{2v} \left\{ 1 + \beta P_2(\cos\theta) P_2\left(\frac{v_Z}{v}\right) \right\} dv \quad (6)$$

where v_{max} is the maximum speed allowed by energy conservation, θ is the angle between the TOF axis and the photolysis electric field vector, $P_2(x)$ denotes the second Legendre polynomial, and β is the anisotropy parameter that characterizes the photodissociation process.

A TOF profile composed by fragments produced from several channels can be fitted as the weighted sum of different CD$_3$ distributions, $F(v_Z,\theta)$, as

$$F(v_Z,\theta) = \sum_i C_i f_i(v_Z,\theta) =$$

$$\sum_i C_i \int_{|v_Z|}^{v_{max}} \frac{g_i(v)}{2v} \left\{ 1 + \beta_i P_2(\cos\theta) P_2\left(\frac{v_Z}{v}\right) \right\} dv \quad (7)$$
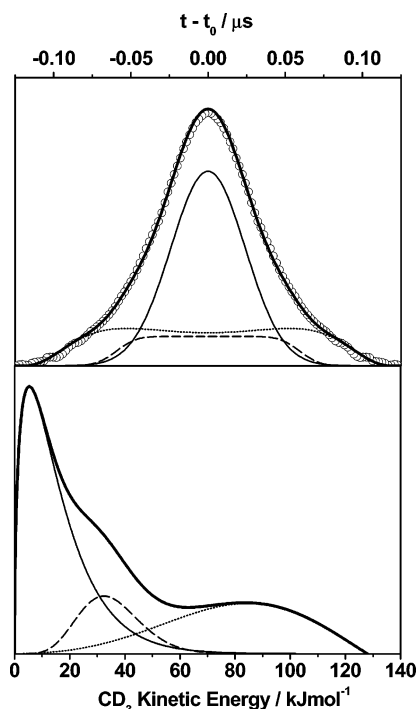
Figure 6. (Top) experimental (circles) and simulated (bold solid line) TOF profiles of the CD_3 fragment after photolysis of DMSO-d_6 using parallel polarized light at 204 nm, showing the contribution of three different channels: internal conversion (solid line), fast dissociation or predissociation (dotted line), and secondary cleavage of CD_3SO (dashed line). (Bottom) energy functions associated to the different distributions mentioned above: isotropic Boltzmann (solid line), anisotropic modified Gaussian (dotted line) and isotropic Gaussian (dashed line).

where C_i is the weight of the ith channel to the total signal. Under space-focusing conditions, v_Z can be calculated as[14]

$$v_Z = \frac{q}{m} E_{\text{ext}}(t-t_0) \qquad (8)$$

where t is the ion arrival time, t_0 is the mean flight time of the ions, q/m is the charge/mass ratio of the detected ion, and E_{ext} is the extraction electric field.

The fitting procedure starts with the TOF profile analysis at both laser polarizations by means of eq 7. Following previous work,[12] the profiles were first fitted using two components. The first component was characterized by a $\beta = 0$ (isotropic) Boltzmann distribution, $P_B(E_t)$, and the second corresponded to a $\beta \neq 0$ (anisotropic) distribution built from a modified Gaussian function of the form[16]

$$P_{\text{MG}}(E_t) =$$
$$NE_t^{3/2}(E_{\text{MG}}^{\text{max}} - E_t) \exp\left(-\left(\frac{E_t - E_0}{\Delta E}\right)^2\right) \qquad E_t \leq E_{\text{MG}}^{\text{max}} \quad (9)$$

where N is a normalization factor, $E_{\text{MG}}^{\text{max}}$ is the maximum kinetic energy of the CD_3 fragment corresponding to the maximum observed time in the TOF profile, and E_0 and ΔE are the parameters of the modified Gaussian function. This type of modified Gaussian distribution has been used to simulate fast dissociation processes with large translational energy release.[16] The fitting parameters were the Boltzmann temperature of the isotropic distribution, the parameters of the modified Gaussian distribution, and their respective weights C_i. For the anisotropic contribution, β was also used as a fitting parameter, because the maximum value of $\tilde{\beta}(t-t_0)$ only represents a lower limit of β.

Despite the wealth of parameter combinations tried in the simulations, it was never possible to fit both the parallel and perpendicular polarization TOF profiles and the $\tilde{\beta}(t-t_0)$ function, simultaneously. Moreover, the fitting procedure was particularly inefficient in the case of the $\tilde{\beta}(t-t_0)$ function for $t - t_0 \approx 0$, except when extremely large widths of the modified Gaussian function were used, which in turn resulted in very bad fitting to the TOF profiles.

The main problem arises from the fact that the Boltzmann distribution dominates the center of the TOF profile, whereas the fast anisotropic signal dominates only on the far *sides* of them, thus leaving a gap that is never perfectly fitted (see Figure 6).

Much better simulations were obtained when a third component was added to the overall fitting procedure. As commented on in section I, a second isotropic type of CD_3 fragments has been observed in several works[8−12] and were assigned to secondary dissociation of the internally hot $CD_3SO(\tilde{X})$, the latter produced in the primary dissociation of the parent molecule. Blank et al.[9] suggested an exit barrier for this channel of at least 33.5 kJ mol^{-1}, which, in principle, can be represented by a Gaussian velocity distribution, which by transformation into relative energy becomes $P_G(E_t)$, the center of which would correspond to the lower limit of the barrier height. Several other functionalities were tried, but only the latter gave good simulations of the profiles. The best simulations were obtained with a maximum of this Gaussian function centered at $E_G^c = 45 \pm 3$ kJ mol^{-1} for all the photolysis wavelengths studied, in good agreement with the lower limit reported by Blank et al.[9]

The lower panel in Figure 6 shows the three kinetic energy distributions of the CD_3 fragments in the center of mass (CM) frame used for the simulation of the TOF profile measured for parallel polarization of the photolysis laser at 204 nm. The upper panel of this figure shows the contribution of each kinetic energy distribution to the TOF profile. The very good agreement found between the simulations and the measured TOF profiles as well as for the $\tilde{\beta}(t-t_0)$ function at all the photolysis wavelengths studied is depicted in Figures 4 and 5.

It has been found that the results obtained from the simulation of the symmetrized TOF profiles are exactly the average between those values determined from the simulations of the left and right parts of the slightly asymmetric raw data, separately. Moreover, the error introduced by the symmetrization procedure is estimated to be within the uncertainties of the parameters characterizing the CM kinetic energy distributions of the different channels.

The CD_3 fragment mean translational energy in the CM frame, $\langle E_t \rangle_{CD_3}$, the C_i weights for each contribution and the β parameter for the anisotropic contribution were extracted from the simulation of the TOF profiles.

To transform the CD_3 translational energy distribution in the CM frame to the relative translational energy distribution, it is necessary to take into consideration the linear momentum conservation. In a two-body dissociation, the relative translational energy $\langle E_t \rangle$ is related to the kinetic energy of a fragment i, $\langle E_t \rangle_i$, by $\langle E_t \rangle = \langle E_t \rangle_i m_p/m_{cf}$, m_{cf} being the mass of the cofragment and m_p the mass of the parent molecule. The secondary decomposition of internally hot $CD_3SO(\tilde{X})$ complicates the application of momentum matching to the fragments. The main problem arises from the fact that $CD_3SO(\tilde{X})$ has an initial velocity as a result of the primary dissociation of the parent molecule. Thus the measured velocity of the secondary CD_3 fragment is the vector sum of the $CD_3SO(\tilde{X})$ initial velocity in the DMSO-d_6 CM frame, $(v_{CD_3SO})_{CM−DMSO}$, plus the CD_3 velocity resulting from the secondary dissociation of $CD_3SO(\tilde{X})$,

UV Photodissociation Dynamics of CD$_3$SOCD$_3$

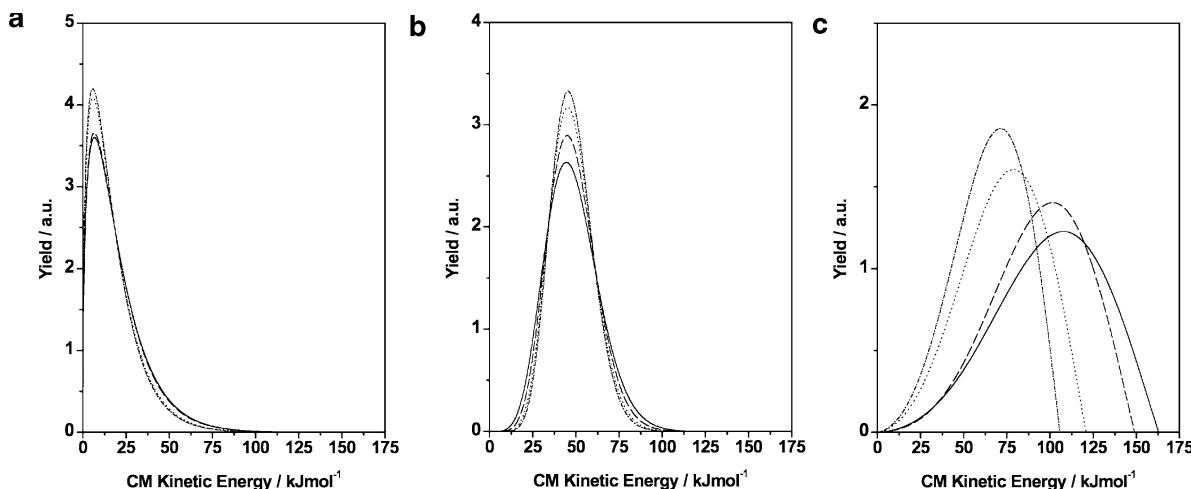*J. Phys. Chem. A, Vol. 108, No. 39, 2004* **8053**

Figure 7. Best fit energy distributions for the three channels producing CD$_3$ fragments at the four photolysis wavelengths studied in this work. All functions are normalized to unity. Left to right: isotropic Boltzmann distribution, isotropic Gaussian distribution, and anisotropic modified Gaussian distribution. For all panels: $\lambda_{pump} = 204$ nm (solid line), $\lambda_{pump} = 210$ nm (dashed line), $\lambda_{pump} = 221$ nm (dotted line), and $\lambda_{pump} = 227$ nm (dashed−dotted line).

TABLE 1: Best Fit Parameters (β, C_i, E_{MG}^{max} and E_G^c), Mean Relative Translational Energies ($\langle E_t \rangle_i$) and Branching Ratios (Γ_i) for Each Dissociation Channel and CD$_3$ Quantum Yield (Φ_{CD_3})

		λ, nm			
		227	221	210	204
primary anisotropic	$\beta \pm 0.05$	0.30	0.31	0.28	0.30
(reaction 4)	$\langle E_t \rangle_{MG} \pm 3$/kJ mol^{-1}	65	73	94	100
modified Gaussian	$E_{MG}^{max} \pm 8$/kJ mol^{-1}	106	121	149	163
$P_{MG}(E_t)$	$C_i \pm 0.01$	0.26	0.26	0.33	0.30
	$\Gamma_4 \pm 0.02$	0.29	0.29	0.38	0.36
	$(E_{avl}^2 - E_{MG}^{max})^a \pm 8$/kJ mol^{-1}	202	203	203	205
primary isotropic	$\langle E_t \rangle_B \pm 2$/kJ mol^{-1}	17	18	20	20
(reaction 2)	$C_i \pm 0.01$	0.64	0.63	0.53	0.54
Boltzmann	$\Gamma_2 \pm 0.03$	0.71	0.71	0.62	0.64
secondary isotropic	$\langle E_t \rangle_G \pm 3$/kJ mol^{-1}	48	48	48	48
(reaction 3)	$E_G^c \pm 2$/kJ mol^{-1}	46	45	45	45
Gaussian	$C_i \pm 0.01$	0.10	0.11	0.14	0.16
$P_G(E_t)$	$C_3/C_2 \pm 0.02^b$	0.16	0.17	0.26	0.30
	$\Phi_{CD_3} \pm 0.03$	1.11	1.12	1.16	1.19

^{a} $E_{avl}^2 = h\nu - \Delta H_2$. ^{b} C_3/C_2 represents the fraction of the CD$_3$SO($\tilde{X}$) formed in reaction 2 that decomposes into CD$_3$ + SO.

namely, the velocity of the secondary CD$_3$ fragment in the CD$_3$SO CM frame, $(\upsilon_{CD_3})_{CM-CD_3SO}$. Of all the studied photolysis wavelengths, the fastest CD$_3$SO($\tilde{X}$) fragments arise after dissociation at 204 nm, this being the less favorable case. At this wavelength, and using the Boltzmann distribution determined for the primary CD$_3$ fragments, the velocity distribution of the CD$_3$SO($\tilde{X}$) can be readily determined by linear momentum conservation. This distribution peaked at ∼295 m/s and extended up to ∼800 m/s. Because the secondary CD$_3$ velocity distribution used in the simulation begins at ∼900 m/s and is centered at ∼1950 m/s, one can assume that the initial velocity of the CD$_3$SO($\tilde{X}$) fragment does not affect considerably the secondary CD$_3$ velocity. Consequently, to obtain the relative kinetic energy distribution, one can neglect the velocity of the primary CD$_3$SO($\tilde{X}$) fragment kinetic energy and SO is used as the momentum matched cofragment.

The relative kinetic energy distributions for the three channels at all the photolysis wavelengths studied are depicted in Figure 7. The values for E_G^c, E_{MG}^{max}, E_t, and C_i for each channel and the β value for the anisotropic one obtained from the best simulation at each photolysis wavelength are shown in Table 1.

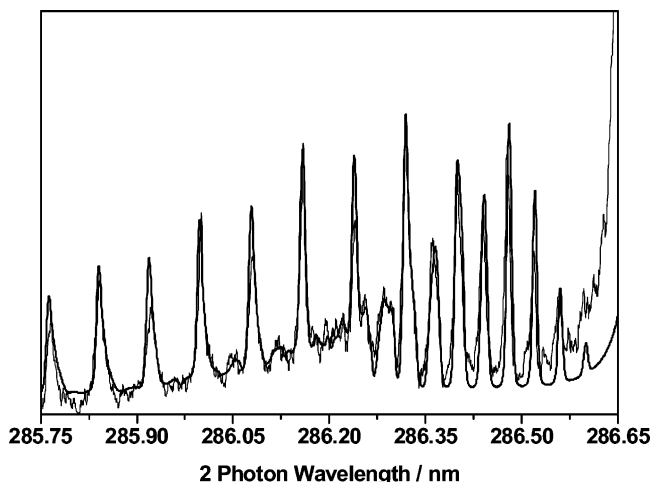**C. CD$_3$ Internal Energy Partitioning and Vibrational State-Resolved Anisotropy Function.** The distribution of the

Figure 8. Experimental (2+1) REMPI rotational spectrum of the nascent CD$_3$ (4p$_z$) ^{2}A$_2''$ ← $\tilde{X}^2$A$_2''$0$_0^0$ after photodissociation of DMSO-d_6 at 221 nm. The simulated spectrum (bold line) is the sum of two contributions with different rotational temperatures, $T_1 = 350$ K (63%) and $T_2 = 90$ K (37%).

internal energy of the fragments can reveal further details on the decomposition mechanism. In this sense, we have recorded rotationally resolved REMPI spectra for the CD$_3$($\upsilon=0$) fragments produced in the DMSO-d_6 photodissociation at 204, 210, 221, and 227 nm, by measuring the 4p$_z$ 0$_0^0$ band. A typical rotationally resolved (2+1) REMPI spectrum is shown in Figure 8 for photodissociation at 221 nm along with the best-fit simulation. Assignments of the R ($\Delta N = +1$) and S ($\Delta N = +2$) rotational branches can be found in ref 12. The O and P branches were not included in the analysis due to contamination of those transitions by the 1$_1^1$ hot band. The simulation procedure employed has been described previously[16] and only a brief account is given here. If N'' and N' denote the rotational quantum numbers of the ground and intermediate resonant states, respectively, and K represents the quantum number of the projection of the rotational angular momentum vector on the C_3 symmetry axis of CD$_3$, the intensity of each $(N',K) \leftarrow (N'',K)$ REMPI rotational transition is given by

$$I_{N'N'',K} = F \frac{S_{N'N'',K}}{(2N''+1)} \frac{1}{D_{N',K}} P_{N'',K} \quad (10)$$
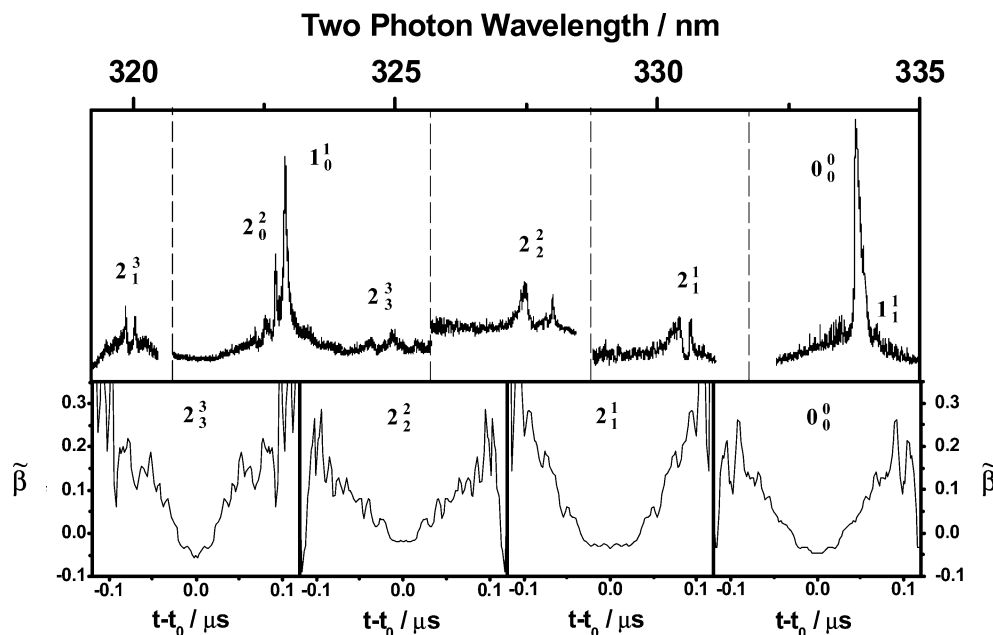
Figure 9. Unnormalized vibrational spectrum of the CD_3 photofragment after dissociation at 204 nm. (Bottom panels) experimental $\tilde{\beta}(t-t_0)$ for four different vibrational bands. In all cases the extraction field was kept low enough to maximize resolution collecting >98.5% of the ions.

TABLE 2: Best Fit Parameters (W_i and T_i) for the CD_3 Rotational Spectra Simulation and CD_3 Mean Rotational Energy $\langle E_R \rangle$

λ, nm	$W_i \pm 0.05$	T_i/K	$\langle E_R \rangle$/kJ mol^{-1}
227	0.64	400 ± 25	5.0 ± 0.3
	0.36	80 ± 10	1.0 ± 0.1
221	0.63	350 ± 25	4.4 ± 0.3
	0.37	90 ± 10	1.1 ± 0.1
210	0.53	600 ± 25	7.5 ± 0.3
	0.47	100 ± 15	1.2 ± 0.2
204	0.50	650 ± 50	8.0 ± 0.6
	0.50	125 ± 25	1.6 ± 0.3

where $S_{N'N'',K}$ are the two-photon line-strength factors for each rotational transition, F is a global scaling factor, and $D_{N',K}$ accounts for the predissociation of electronically excited CD_3, which for the $4p_z$ $^2A_2''$ state in the ground vibrational state is dominated by rotation−translation Coriolis coupling. Finally, $P_{N'',K}$ stands for the relative population of each (N'',K) rotational level of the ground-state CD_3, including the nuclear spin degeneracy

$$P_{N'',K} = \frac{G_K(2N'' + 1)}{Q(T_{N''})} \exp\left[-\frac{E(N'',K)}{k_B T_{N''}}\right] \qquad (11)$$

where $Q(T_{N''})$ is the rotational partition function, k_B is the Boltzmann constant, and $T_{N''}$ is the rotational temperature of the CD_3 ground electronic state. The nuclear spin degeneracy, G_K, is equal to 1 and 10 for N'' even and odd and $K = 0$, respectively, and follows the progression 8, 8, 11, 8, 8, 11, ..., for $|K| = 1, 2, 3, 4, ...$ ($|K| \leq N''$).

A first attempt to simulate the measured REMPI spectra was performed by assuming a unique Boltzmann distribution characterized by a single temperature $T_{N''}$. However, it was not possible to obtain good agreement between the experimental and simulated spectra. In line with the TOF profile analysis (see section III.B), we performed a simulation assuming more than one Boltzmann distribution, each of them characterized by a temperature $T_{N''}$ and a weighting factor W_i. Figure 8 shows the best simulation obtained using two Boltzmann distributions. Good results were also obtained when using three Boltzmann

distributions, but considering experimental errors and the accuracy of the results, the presence of a third contribution to the rotational spectrum is not sufficiently clear.

The fitting parameters ($T_{N''}$ and W_i) for the simulations carried out at all the photolysis wavelengths studied using two Boltzmann distributions are shown in Table 2. Note that the weighting factor W_i for the component with the highest temperature, at each photolysis wavelength, approximates the C_i value of the corresponding primary isotropic channel obtained from the TOF profiles analysis (see Table 1). On the other hand, W_i for the component with the lowest temperature agrees, within the experimental error, with the sum of the contributions of the secondary isotropic and the primary anisotropic channels.

Figure 9 shows the nascent CD_3 vibrational spectrum arising from the photodissociation of DMSO-d_6 at 204 nm, recorded in the $3p_z$ $^2A_2'' \leftarrow \tilde{X}^2A_2''$ transition. We were able to assign several vibrational bands in the spectrum, i.e., 0_0^0, 1_0^1, 1_1^1, 2_0^2, 2_1^1, 2_1^3, 2_2^2, and 2_3^3. As can be seen, most of the bands correspond to excitation of the ν_2 (umbrella) mode (up to $v = 3$), and of the ν_1 (stretching) mode ($v = 0, 1$). The fact that ν_2 is the most active vibrational mode of the CD_3 fragment in the photodissociation of DMSO-d_6 is not too surprising. The CD_3 groups in the parent molecule are of pyramidal geometry, whereas the product CD_3 is planar. Thus, the umbrella motion of the CD_3 moiety couples favorably to the reaction coordinate. Although the determination of the vibrational distribution is subject to a considerable error, the present analysis suggests a minimum vibrational energy content of about 10 kJ mol^{-1} in the ν_2 vibrational mode of CD_3. The presence of a CD_3 ν_1 vibrational excitation is not surprising because the predominant primary dissociation channel occurs on the ground state via internal conversion from the originally excited electronic state and thus it is statistical. Accordingly, there is enough time for vibrational energy redistribution and one of the appearing excited modes of the CD_3 fragment is the stretching.

The dependence of the CD_3 TOF profiles on the photolysis laser polarization angle was investigated at 204 nm for several selected vibrational transitions, i.e., 2_1^1, 2_2^2, and 2_3^3, in addition to the 0_0^0 reported in section III.B. The bottom panels in Figure 9 show the results of the $\tilde{\beta}(t-t_0)$ function for each vibrational

TABLE 3: Available Energy and Product Energy Partitioning, $\langle f_t \rangle_i$ and $\langle f_{R+V} \rangle_i$, for Each of the Three Dissociation Channels, at the Four Photolysis Wavelengths Studied in This Work^a

	λ			
	227 nm	221 nm	210 nm	204 nm
Primary Anisotropic Channel (Reaction 4)				
$(E^4_{avl})^b$/kJ mol^{-1}	104	121	149	164
$\langle f_t \rangle_{MG}$	0.63	0.60	0.63	0.61
$\langle f_{R+V} \rangle_{CD_3} \leq$	0.10	0.09	0.08	0.07
$\langle f_{R+V} \rangle_{CD_3SO(\tilde{A})} \geq$	0.27	0.31	0.29	0.32
Primary Isotropic Channel (Reaction 2)				
(E^2_{avl})/kJ mol^{-1}	307.5	324.2	351.8	367.7
$\langle f_t \rangle_B$	0.05	0.06	0.06	0.05
$\langle f_{R+V} \rangle_{CD_3} \leq$	0.05	0.04	0.05	0.05
$\langle f_{R+V} \rangle_{CD_3SO(\tilde{X})} \geq$	0.90	0.90	0.89	0.90
Secondary Isotropic Channel (Reaction 3)				
(E^3_{avl})/kJ mol^{-1}	94.5	111.2	138.8	154.7
$\langle f_t \rangle_G$	0.51	0.43	0.35	0.31
$\langle f_{R+V} \rangle_{CD_3} \leq$	0.11	0.10	0.08	0.07
$\langle f_{R+V} \rangle_{SO} \geq$	0.38	0.47	0.57	0.62

^{a} The symbols $\leq$ and $\geq$ indicate lower and upper limit values, respectively. ^{b} $E^3_{avl} = h\nu - \Delta H_2 - \langle E_{CD_3SO(\tilde{A})} \rangle$. See text for details.

transition. There are two significant points to be highlighted from this figure: (i) the $\tilde{\beta}(t-t_0)$ function in the 0^0_0 transition is independent of the intermediate CD$_3$ Rydberg state (3p$_z$ or 4p$_z$) used in the detection REMPI scheme (see left bottom panel in Figure 4), and (ii) the maximum value of the $\tilde{\beta}(t-t_0)$ function is roughly the same for all levels ($v = 0-3$) of the ν_2 mode within the experimental uncertainty. This indicates that the anisotropy parameter β and the percentage of anisotropic channel are almost independent of the CD$_3$ photofragment vibrational excitation.

IV. Discussion

A first consideration is whether the present results for the photodissociation of DMSO-d_6 are consistent with a concerted cleveage of the two C–S bonds. All attempts to explain the energy distributions obtained from the simulations of the measured TOF profiles for the different CD$_3$ fragments by resorting to a concerted mechanism were unsuccessful. In fact, assuming a three-body concerted dissociation the maximum relative energy in the CM frame, E^{max}_{CM}, was about twice that of the available energy considering the dissociation energy of the two C–S bonds (reaction 1) and the photon energy.

In what follows, we will discuss the different dissociation channels found in the analysis of the experimental results.

A. Primary Slow Isotropic Channel and Secondary Dissociation. The relative kinetic energy distributions for the primary isotropic channel, $P_B(E_t)$, at all the photolysis wavelengths studied are depicted in Figure 7a. These $P_B(E_t)$ peak at ≈ 10 kJ mol^{-1} and decrease exponentially out beyond 100–110 kJ mol^{-1}. This type of distribution peaking near zero and with an exponential decreasing tail is characteristic of a statistical dissociation involving little or no recombination barrier.[9] These CD$_3$ fragments may result from reaction 2, which is extensively accepted to occur on the ground electronic surface after IC from the originally excited state of DMSO-d_6.[9–12]

The available energy E_{avl} for this channel ranges from 307.5 kJ mol^{-1} at 227 nm to 367.7 kJ mol^{-1} at 204 nm. Table 3 shows the fraction of E_{avl} going into recoil energy of the fragments, $\langle f_t \rangle_B$. The small values determined at all the photolysis wavelengths ($\langle f_t \rangle_B \leq 0.06$) are in close agreement with those reported
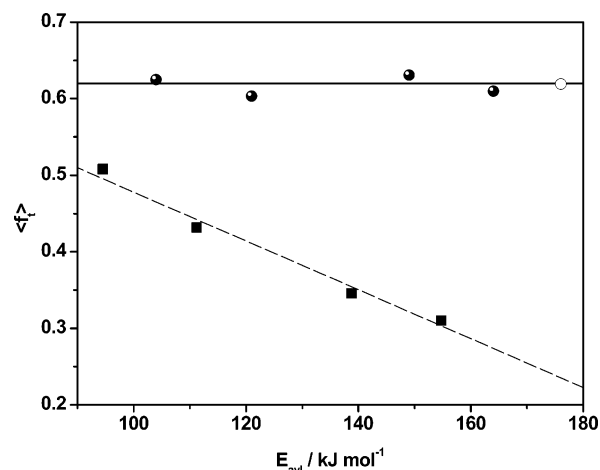

Figure 10. (Circles) translational energy fraction as a function of the available energy for the primary anisotropic CD$_3$ fragments. (Filled circles) values from best fit obtained in this work. (Open circle) value determined by Blank et al.[9] (Solid line) impulsive model (ref 19). (Filled squares) best fit translational energy fraction as a function of the available energy for the secondary CD$_3$ fragments. The dashed line is displayed as a visual guide.

by Thorson et al.[11] at 210 and 222 nm, as well as with prior model calculations for this channel.[11]

As mentioned in section III.C, a comparison of the W_i weights obtained from the simulation of the rotational REMPI spectra with the C_i weights obtained from the simulation of the TOF profiles indicates a close correlation between the highest rotational temperature and the Boltzmann type translational distribution, $P_B(E_t)$. Therefore, the CD$_3$ fragments arising from reaction 2 are generated with high rotational temperature and the mean rotational energies $\langle E_R \rangle$ shown in Table 2. The determination of an accurate mean vibrational energy $\langle E_V \rangle$ has not been possible in the present experiments and only a rough approximated value, averaged over all the CD$_3$ channels, of $\langle E_V \rangle$ ≈ 10 kJ mol^{-1} has been used. In line with Blank et al.[9] and Rudolph et al.,[10] this value may be considered as a lower limit for CD$_3$ arising from channel 2. However, the implicit error of this approximation does not change the main conclusions.

The E_{avl} partitioned into internal energy of the cofragment CD$_3$SO($\tilde{X}$), $\langle f_{R+V} \rangle_{CD_3SO(\tilde{X})}$, calculated from energy conservation at the different photolysis wavelengths are presented in Table 3. The fact that a large amount of E_{avl} is channeled into the internal degrees of freedom of CD$_3$SO($\tilde{X}$) is consistent with the subsequent secondary decomposition (reaction 3) previously proposed by several authors.[8–12] The recoil energy distributions for the secondary channel, $P_G(E_t)$, are shown in Figure 7b. These distributions differ significantly from the Boltzmann type distributions shown in Figure 7a in that they are bell-shaped and not centered near zero. In addition, the distributions are barely sensitive to the excitation energy. This suggests that the secondary dissociation dynamics is mediated by a substantial exit barrier, the height of the barrier being close to the maximum of the $P_G(E_t)$.[2,9,17] This implies that for this channel $\langle f_t \rangle_G$ should decrease as E_{avl} increases, as shown in Figure 10 (square symbols). A plausible mechanism would involve intramolecular vibrational energy redistribution (IVR) prior to dissociation, in which the repulsive forces acting beyond the transition state dominate the translational energy release. Dissociation would only happen if sufficient energy flows into the reaction coordinate to overcome the exit barrier. As available energy increases, there will be more energy channeled into product translational energy, but this effect will be small compared to

the large translational energy release originated from the exit barrier, and this will only affect the width of $P_G(E_t)$.[2,9,17]

From the analysis of the TOF profiles it is possible to infer a value of the reverse recombination barrier of 45 ± 2 kJ mol^{-1}, which is in good agreement with those reported by Blank et al.[9] (>33.5 kJ mol^{-1}) and by Thorson et al.[11] (39 ± 4 kJ mol^{-1}).

The assignment of the lowest rotational temperatures obtained from the simulation of the rotational REMPI spectra to the CD$_3$ fragments generated in the secondary dissociation is consistent with the estimations by Blank et al.[9] and Rudolph et al.[10] of a very little energy remaining in the internal degrees of freedom of the methyl radical. As a consequence, from energy conservation, the mean internal energy of the SO fragment, $\langle E_{R+V}\rangle_{SO}$, should be in the range $36-96$ kJ mol^{-1} as the photolysis wavelength decreases from 227 to 204 nm (see Table 3). In addition, Thorson et al.[11] have determined a value of $\langle E_{R+V}\rangle_{SO} \approx 22$ kJ mol^{-1} at 222 and 210 nm photodissociation wavelength, whereas Blank et al.[9] and Chen et al.[7] reported a value of $\langle E_{R+V}\rangle_{SO} \approx 38$ kJ mol^{-1} at 193 nm. The possible discrepancies can arise from the fact that the present estimated value of $\langle E_V\rangle_{CD_3} \approx 10$ kJ mol^{-1} is a lower limit of the actual value.

B. Primary Fast Anisotropic Channel. The deduced relative translational energy distributions for this channel, $P_{MG}(E_t)$, are shown in Figure 7c at all the photolysis wavelengths studied. The main differences of these distributions compared with those of the two other channels (see Figure 7a,b) are the large variation of the position of the peak and the maximum energy (E_{MG}^{max}) of the distributions with the photon energy and, thus, of $\langle E_t\rangle_{MG}$ (see Table 1). Assuming that E_{MG}^{max} corresponds to the production of vibrationally and rotationally cold CD$_3$SO fragments, and considering that vibrationless CD$_3$ fragments are probed in this experiments (Q 0^0_0), E_{MG}^{max} would have to be the E_{avl} after absorption of one photon. However, this value is ≈ 200 kJ mol^{-1} smaller than the available energy corresponding to reaction 2, E_{avl}^2 (307.5$-$367.7 kJ mol^{-1}), calculated using $\Delta H_2 = 218$ kJ mol^{-1} for this reaction.[5] In agreement with previous works,[9,12] the explanation of this apparent discrepancy is that the anisotropic CD$_3$ fragments do not arise from reaction 2 but from reaction 4, in which electronically excited CD$_3$SO(Ã) is produced. The energy of this excited state can be determined from the difference $E_{avl}^2 - E_{MG}^{max}$ at each photolysis wavelength (see Table 1), resulting in an average value of 203 ± 8 kJ mol^{-1}, in good agreement with the value of 225 kJ mol^{-1} reported by Blank et al.[9] A value of ≈ 200 kJ mol^{-1} for CD$_3$SO(Ã) renders $\langle f_t\rangle_{MG} \approx 0.60$ at all photolysis wavelengths, consistent with a direct dissociation on a repulsive electronic surface or electronic predissociation with another repulsive surface.

Electronic predissociation does not seem to take place through an exit barrier originated by an avoided crossing on the originally excited state (as in the case of acetone[2] or dimethyl sulfide in the first absorption band[18]) because the maximum of the $P_{MG}(E_t)$ clearly changes with the photolysis energy (see Figure 7c). A plot of $\langle f_t\rangle$ vs E_{avl} yields a zero slope straight line, as expected for an impulsive dissociation. Furthermore, a simple calculation with a soft impulsive model of energy partitioning into translational and internal degrees of freedom of the photofragments in the limit of a prompt dissociation (modified by Trentelman et al.[19]), predicts a value of $\langle f_t\rangle_{MG} = 0.62$ (solid line in Figure 10). These evidences suggest that the mechanism responsible for the anisotropic channel is either a direct dissociation over a repulsive surface or a fast predissociation with a repulsive electronic state. In any case, the repulsive surface should correlate adiabatically with CD$_3$SO(Ã) and CD$_3$(X̃) fragments. In the case of a direct dissociation, the

fact that only 29$-$38% of the primary CD$_3$ fragments are formed via this channel would indicate that the repulsive surface is not the same electronic state that undergoes IC to the ground state (channel 2).

Interestingly, Blank et al.[9] also obtained a value of $\langle f_t\rangle_{MG} \approx 0.62$ at 193 nm (open circle in Figure 10), although the initial excitation was to a different DMSO-d_6 electronic state. Therefore, it might be possible that it is the same *dark* DMSO excited state that (pre)dissociates the upper states in the $193-227$ nm excitation wavelength range. Because there is little theoretical information on the DMSO, we do not know the nature of the repulsive electronic state. Due to the impulsive nature of the dissociation, it is very likely that this state has C$-$S antibonding character.

Such an impulsive photodissociation cannot induce rotation into the fragment, because the force is directed along the S$-$C reaction coordinate toward the CM of the CD$_3$ fragment.[19] Thus the lowest rotational temperature extracted from the rotational REMPI spectra can be assigned to the CD$_3$ fragments resulting from this channel. Table 3 shows that $\langle f_{R+V}\rangle_{CD_3} \leq 0.10$ and that about 30% of the available energy goes into internal excitation of the CD$_3$SO(Ã) cofragment. Blank et al.[9] have proposed that this electronically excited fragment is long-lived, because it is produced internally colder than the CD$_3$SO(X̃) formed in reaction 2. This electronically excited fragment may undergo a radiative decay, because nonradiative relaxation would result in vibrational excitation, which was not evidenced in the experiments of ref 9. Thus, CD$_3$SO(Ã) cannot decompose to SO and secondary CD$_3$ fragments as in the case of CD$_3$SO(X̃).

Although the excited state of the parent molecule may be long-lived enough to redistribute some of the available energy among the vibrational$-$rotational modes, the event occurs before the angular distribution information is smeared out by the rotational motion of the molecule, as determined by the anisotropy parameter. Although fast CD$_3$ fragments from a prompt dissociation process were detected at 193 nm, spatial anisotropy of the signal was not observed, mostly due to signal-to-noise limitations.[9] The best fit value of the anisotropy parameter $\beta = 0.30 \pm 0.05$, determined in this work, indicates a parallel transition and it actually represents a lower limit of the real β due to the lifetime of the excited state.[20] Simple considerations based on the symmetry and geometry of the molecule and assuming a prompt recoil along the CS$-$C axis yield positive values of $\beta = 0.7$ and 0.34 for the transition moment along the x and z axes, respectively, in the body fixed frame. The latter is quite close to the present experimental result, which may be fortituous. However, due to the excited state lifetime considerations previously discussed and the uncertainties in the DMSO excited-state geometry, the former value of 0.7 cannot be ruled out.

C. Branching Ratios and Quantum Yields. The primary dissociation branching ratio is defined as $\Gamma_i = C_i/\Sigma_j C_j$, where C_i (taken from Table 1) represents the weight of the two primary dissociation channels (reactions 2 and 4) to the total TOF profile. For the primary anisotropic channel (reaction 4), Γ_3 ranges from 0.29 at 227 nm to 0.36 at 204 nm (see Table 1) with a maximum of 0.38 at 210 nm. Although, presumably, this is not an actual maximum, the value determined by Blank et al.[9] at 193 nm (0.27) follows the same tendency.

On the basis of these weights, the CD$_3$ quantum yield can be calculated. If reactions 2 and 4 are the primary dissociation channels, the sum of the CD$_3$ from each of them must result in $\Phi_{CD_3} = 1.0$. However, if a percentage of the CD$_3$SO(X̃) formed in reaction 2 decomposes to CD$_3$ and SO via reaction 3, then
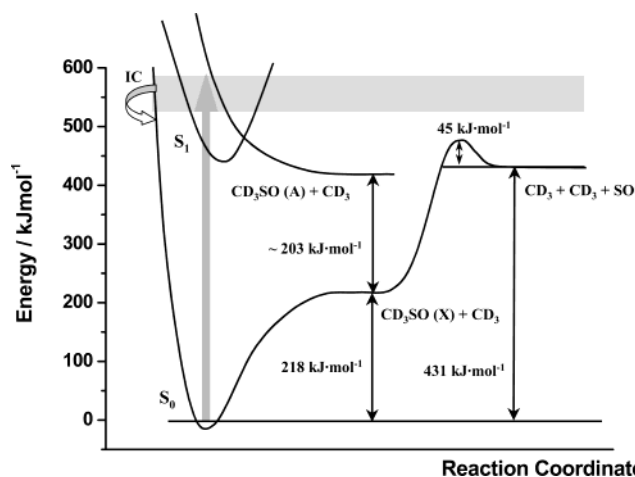
Figure 11. Schematic representation of the overall mechanism for the photodissociation of DMSO-d_6. Energy vs reaction coordinate diagram based on thermodynamics data taken from ref 6. See text for details.

the Φ_{CD_3} must be larger than 1. The calculated $\Phi_{CD_3} = 1.11-$ 1.19 are shown in Table 1 at each of the photolysis wavelengths of this work.

Note that the value at 221 nm ($\Phi_{CD_3} = 1.12$) is in very good agreement with those reported by Thorson et al.[11] and Rudolph et al.[10] (1.1 ± 0.1 and 1.2 ± 0.2, respectively). At 210 nm, the present value ($\Phi_{CD_3} = 1.16$) is close to that reported by Thorson et al.[11] (1.3 ± 0.1). However, their value must be taken as an upper limit, due to the loss of the fast primary CD$_3$ fragments in their experiments (see ref 12). Finally, a compilation of all works done on DMSO photodissociation at 193 nm shows an increase of Φ_{CD_3} with photon energy up to 1.4 for DMSO-d_6[9] and 1.53 for DMSO-h_6.[8,9] The same behavior has been observed in the present work. Although Φ_{CD_3} seems to be practically constant within the experimental error, this effect is due to the increase of Γ_4 and the consequent decrease of Γ_2 as photon energy increases. However, it must be noted that the fraction of CD$_3$SO($\tilde{X}$) that decomposes to produce secondary CD$_3$ fragments, C_3/C_2 (shown in Table 1), really increases with photon energy from 0.16 at 227 nm up to 0.30 at 204 nm.

The present results can be summarized with a schematic energy diagram of the overall dissociation, including all the observed dissociation channels and the estimated exit barrier for reaction 3, as shown in Figure 11.

V. Conclusions

The photodissociation dynamics of DMSO-d_6 has been studied in the UV (204−227 nm) using the REMPI-TOF technique to investigate the internal and translational energy disposal into the CD$_3$ photofragment.

Evidence for a stepwise mechanism for the major dissociation channel has been found. The primary dissociation (reaction 2) proceeds after internal conversion to the ground state over little or no barrier, resulting in statistical energy partitioning in translation, with most of the available energy channeled into the internal degrees of freedom of CD$_3$SO($\tilde{X}$). If CD$_3$SO($\tilde{X}$) is produced with sufficient internal energy to overcome the barrier for the C−S bond cleavage, it decomposes to SO and secondary CD$_3$ fragments (reaction 3). The secondary CD$_3$ yield increases with the available energy, and the translational energy distribution for this channel indicates the presence of an exit barrier ($\approx$45 kJ mol^{-1}) in good agreement with previous works.

In addition, experimental evidence has been found for a competing channel in the primary dissociation in which electronically excited CD$_3$SO($\tilde{A}$) is produced. A careful analysis of the TOF profiles has shown that CD$_3$ fragments from reaction 4 were spatially anisotropic with $\beta = 0.30 \pm 0.05$, in accordance with a parallel transition.

Moreover, 62% of the available energy for this channel is partitioned into center-of-mass translational energy, which agrees with a fast dissociation (direct dissociation or predissociation) from the excited electronic state to a repulsive surface. The latter value is also consistent with the data at 193 nm, previously published, in which 62% of the available energy appears as translational energy of the products, in agreement with a soft impulsive model.

References and Notes

(1) Strauss, C. E. M.; Houston, P. L. *J. Phys. Chem.* **1990**, *94*, 8751.
(2) North, S. W.; Blank, D. A.; Gezelter, J. D.; Longfellow, Ch. A.; Lee, Y. T. *J. Chem. Phys.* **1995**, *102*, 4447.
(3) Kim, S. K.; Pedersen, S.; Zewail, A. H. *J. Chem. Phys.* **1995**, *103*, 477.
(4) Barnes, I.; Becker, K. H.; Carlier, P.; Mouvier, G. *Int. J. Chem. Kinet.* **1987**, *19*, 489.
(5) The heats of formation were taken from: *CRC Handbook of Physics and Chemistry*; CRC: Cleveland, 1985. Lias, S. G.; Bartmess, J. E.; Liebman, J. F.; Holmes, J. L.; Levine, R. D.; Mallard, W. G. *Phys. Chem. Ref. Data* **1988**, 17. Benson, S. W. *Chem. Rev.* **1978**, *78*, 23.
(6) Gollnick, K.; Stracke, H. *Pure Appl. Chem.* **1973**, *33*, 217.
(7) Chen, X.; Wang, H.; Weiner, B. R.; Hawley, M.; Nelson, H. H. *J. Phys. Chem.* **1993**, *97*, 12269.
(8) Zhao, H.-Q.; Cheung, Y.-S.; Heck, D. P.; Ng, C. Y.; Tetzlaff, T.; Jenks, W. S. *J. Chem. Phys.* **1997**, *106*, 86.
(9) Blank, D. A.; North, S. W.; Stranges, D.; Suits, A. G.; Lee, Y. T. *J. Chem. Phys.* **1997**, *106*, 539.
(10) Rudolph, R. N.; North, S. W.; Hall, G. E.; Sears, T. J. *J. Chem. Phys.* **1997**, *106*, 1346.
(11) Thorson, G. M.; Cheatum, Ch. M.; Coffey, M. J.; Crim, F. *J. Chem. Phys.* **1999**, *110*, 10843.
(12) Amaral, G. A.; Torres, I.; Pino, G. A.; Aoiz, F. J.; Bañares, L. *Chem. Phys. Lett.* **2004**, *386*, 419.
(13) Barr, J.; Torres, I.; Bañares, L.; Verdasco, J. E.; Aoiz, F. J. *Chem. Phys. Lett.* **2003**, *373*, 550.
(14) Wiley, W. C.; McLaren, I. H. *Rev. Sci. Instrum.* **1955**, *26*, 1150.
(15) Simion 3-D. Version 6.0. *Idaho National Engineering Laboratory.* E. G. & G. Idaho Inc., Idaho Falls, ID, 1987.
(16) Martínez-Haya, B.; Aoiz, F. J.; Bañares, L.; Quintana, P.; Verdasco, E. *J. Phys. Chem. A* **2000**, *104*, 10150.
(17) Mordaunt, D. H.; Osborn, D. L.; Neumark, D. M. *J. Chem. Phys.* **1998**, *108*, 2448.
(18) Barr, J.; Torres, I.; Verdasco, E.; Bañares, L.; Aoiz, F. J.; Martínez-Haya, B. *J. Phys. Chem. A* **2004**, *108*, 7936.
(19) Trentelman, K. A.; Kable, S. H.; Moss, D. B.; Houston, P. L. *J. Chem. Phys.* **1989**, *91*, 7498.
(20) Yang, S.-Ch.; Bersohn, R. *J. Chem. Phys.* **1974**, *61*, 440.